Integrated large-eddy simulation for modeling plant-tissue warming induced by wind machines in an orchard canopy

Dai, Yi; van Hooft, Antoon; Patton, Edward G.; Boekee, Judith; van der Linden, Steven; ten Veldhuis, Marie Claire; van de Wiel, Bas J.H.

DOI
10.1016/j.agrformet.2024.110175

Publication date
2024

Document Version
Final published version

Published in
Agricultural and Forest Meteorology

Agricultural and Forest Meteorology 356 (2024) 110175

Contents lists available at ScienceDirect

Agricultural and Forest Meteorology

journal homepage: www.elsevier.com/locate/agrformet

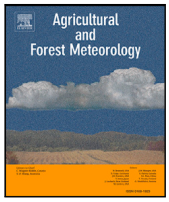

Integrated large-eddy simulation for modeling plant-tissue warming induced by wind machines in an orchard canopy

Yi Dai [a,*], Antoon van Hooft [b], Edward G. Patton [d], Judith Boekee [c], Steven van der Linden [a], Marie-Claire ten Veldhuis [c], Bas J.H. van de Wiel [a]

[a] Faculty of Civil Engineering and Geosciences, Department of Geoscience and Remote Sensing, Delft University of Technology, Stevinweg 1, Delft, 2628CN, The Netherlands
[b] Department of Biomedical Engineering, Eindhoven University of Technology, De Zaale, Eindhoven, 5600MB, The Netherlands
[c] Faculty of Civil Engineering and Geosciences, Department of Water Management, Delft University of Technology, Stevinweg 1, Delft, 2628CN, The Netherlands
[d] National Center for Atmospheric Research, Boulder, CO, USA

ARTICLE INFO

Dataset link: github

Keywords:
Frost mitigation
Canopy modeling
Plant-tissue temperature
Wind machines
Large-eddy simulation

ABSTRACT

Wind machines are increasingly used to mitigate spring frost damage in agricultural sectors. Complementing quasi-3D temperature measurements to quantify the warming effects of wind machines (Dai et al., 2023), this study develops a numerical model to quantify warming effects on air and plant tissues and resolve the dynamic interplay between turbulent rotating plumes and canopy structure. We implement an integrated model in a large-eddy simulation and validate the model against field observations. Simulation results show remarkable agreement with the air mixing and warming effects observed during wind machine operation in Dai et al. (2023). Simulation results reveal significant air and leaf warming near the wind machine due to direct jet-mixing. Beyond 20 m from the machine (3–4 rotor diameters), while wind velocities drop rapidly, the warming is sustained and gradually decreases over distance. This sustained warming, without direct jet mixing, likely results from the advection of jet-entrained warm air. The warming extends 150 m upstream and 550 m downstream, influenced by the background wind. This difference is attributed to the interaction between the machine-induced jet and the background wind, forming convergence patterns when jets oppose the wind and extended warming plumes in wave-like patterns when jets align with the wind. Cross-stream warming symmetrically extends about 250 m. Within these warming regions, leaf temperatures closely follow air temperatures due to strong turbulent heat exchanges. Outside the warming zone, radiative cooling prevails, bringing the leaf–air temperature difference back to approximately 1 degree. These findings collectively give new insights into interactions between the induced warming plumes and air flows within the canopy and provide a useful tool to optimize operational wind machine deployment. This integrated model uniquely provides a full, multi-process representation of outdoor reality with respect to wind machine operation in orchards.

1. Introduction

Spring frost events can lead to significant economic losses in the agricultural sector (Lamichhane, 2021). To combat frost damage, wind machines (hereafter WMs) have become increasingly popular (Frith, 1951). During radiative frost nights[1], WMs generate strong jets and erode the near-surface thermal inversion through air mixing. This mixing process enhances both vertical air-to-air and local plant–air heat exchange, resulting in elevated plant-tissue temperatures. Understanding the dynamics of air mixing and their effects on plant-tissue temperatures is essential for optimizing WM operations.

Quantifying warming effects on plant tissues requires understanding the processes of vertical air-to-air mixing and local plant–air heat exchange. The air-to-air mixing effects highly depend on machine type (e.g., power, blades, hub height), operational settings (e.g., rotation period, tilting angle), and atmospheric conditions (e.g., inversion strength, wind speed) (Table 1 in Dai et al. 2023). Air-to-air mixing

* Corresponding author.
E-mail address: Y.Dai-1@tudelft.nl (Y. Dai).

[1] Radiation frost occurs with clear skies and calm winds, forming a temperature inversion near the surface, while an advective freeze happens when a cold air mass moves in, bringing freezing temperatures. WMs likely work better during radiative frost nights.

https://doi.org/10.1016/j.agrformet.2024.110175
Received 24 April 2024; Received in revised form 17 July 2024; Accepted 23 July 2024
Available online 30 July 2024

effects are spatially and temporally complex due to 360° rotation of the WM and interaction between the generated turbulent warming plumes and the non-uniform canopy structure. Locally, heat exchange processes depend on in-canopy air temperature, wind velocity and canopy characteristics. Furthermore, the distribution of mean wind and turbulence within the canopy airspace is also closely linked to the canopy structure. As a result, assessing the warming impact on plant tissues across the orchard is a challenging task.

Current physical understanding of the complex interactions of machine-induced warming of plant tissues remains limited. Experimental studies often face challenges with the coverage and resolution of measurements, which are typically insufficient to fully capture the temporal and spatial variability of machine-induced air mixing in orchards (e.g., Ribeiro et al., 2006; Battany, 2012; Kimura et al., 2017; Beyá-Marshall et al., 2019). Furthermore, there are only a few numerical studies available. Heusinkveld et al. (2020) simulated machine-induced air mixing using an actuator disk model and estimated air warming based on Gaussian curve fittings. Yet their study did not incorporate canopy effects, such as canopy drag and canopy–air heat exchange. The dynamic interplay between turbulent warming plumes and canopy structure, as well as the heterogeneous plant–air heat exchange in the orchard, has not been investigated numerically so far.

The field experiment conducted by our group (Dai et al., 2023) measured the air mixing effects of WM operation in a 6.75 ha orchard block. Dai et al. (2023) obtained quasi-3D air temperature responses with spatial-sampling and temporal resolution of 25 cm and 10 s, respectively, before and during WM operation. The current study is complementary to the field study: it aims to develop a numerical model for quantifying warming effects on plant tissues as well as resolving the dynamic interplay between turbulent rotating plumes and canopy structure. We implement an integrated model in a large-eddy simulation and validate the model against the field observations (Dai et al., 2023). The integrated model incorporates a canopy model, an air–plant–tissue heat exchange model, and a wind machine model. The canopy model parameterizes the effect of orchard tree lanes on flow dynamics. We adapted the parameterization for horizontally-homogeneous canopies from Patton et al. (2016). We integrate a conceptual energy balance model to investigate the local air–plant–tissue heat exchange processes and to simulate plant-tissue temperature dynamics (Boekee et al., 2023). Additionally, the WM operation is parameterized using an actuator disk approach following Heusinkveld et al. (2020). A detailed description of the LES and the integrated model is provided in Section 2. The simulation settings for reproducing the experimental conditions are explained in Section 3. We compare the simulated results with field data previously reported in Dai et al. (2023). Using a total of 9 km of fiber optic cable, their study measured quasi-3D temperature responses with a spatial sampling of 25 cm and a temporal resolution of 10 s over a 6.75 ha orchard. Specifically, we compare simulation results with measurements taken at a 9 m tower and a horizontal slice over a 6.75 ha orchard at 2 m height. The comparison between the measurements and simulation results is presented in Section 4.1. To further explore the air mixing effect across the orchard, simulated temperature and wind profiles are examined in Section 4.2. Section 4.3 explores the mixing dynamics up- and downstream. The conclusion and recommendation for future work are given in Section 5.

2. The integrated model

2.1. The large-eddy simulation

The large-eddy simulation is based on Basilisk, a partial-differential-equation solver, which solves the equations of atmospheric boundary layer under the Boussinesq approximation on adaptive Cartesian grids. The application of adaptive mesh refinement (AMR) for studying turbulent atmospheric flows is well-documented in the literature (Van Hooft et al., 2018; van Hooft et al., 2019; Heusinkveld et al., 2020). The AMR method dynamically refines and coarsens the grid size in space and time based on the characteristics of the local flow field. Specifically, the mesh adjusts its refinement levels by comparing the local discretized error to a prescribed refinement threshold. The AMR method in Basilisk used for current study is expected to resolve the presence of orchard tree lanes and the WM using minimum grid size, while coarsening the grid in the less turbulent areas. Thus, employing AMR is expected to enhance computational efficiency (Van Hooft et al., 2018; Heusinkveld et al., 2020). The grid setting near the canopy and WM is detailed in Fig. 2, Section 3. The LES filtered equations for momentum $\mathbf{u} = (u_1, u_2, u_3)$ in (x, y, z) directions and buoyancy (b) are solved numerically. Parameterization of canopy processes (F_d, S_b) and the WM forcing (U_M) are discussed in Section 2.2 and 2.3, respectively.

$$\frac{\partial \widetilde{u_i}}{\partial t} + \frac{\partial \widetilde{u_j}\widetilde{u_i}}{\partial x_j} = -\frac{\partial \pi}{\partial x_i} + \widetilde{b}\delta_{i3} - \frac{\partial \tau_{ij}}{\partial x_i} - \frac{\partial p_{LS}}{\partial x_i} + F_d + U_M, \tag{1}$$

$$\frac{\partial \widetilde{b}}{\partial t} + \frac{\partial \widetilde{u_j}\widetilde{b}}{\partial x_j} = -\frac{\partial B_j}{\partial x_j} + S_b, \tag{2}$$

where the tildes denote the spatial filtered variables. π represents the modified pressure and δ_{i3} is the Kronecker delta. The large-scale forcing is imposed by the pressure (p_{LS}) gradient term. The Coriolis force is not included due to the small domain scale and short simulation time. We adhere to the Basilisk convention for solving buoyancy terms (b), which is the same as solving for potential temperatures θ as they vary linearly,

$$b = \frac{g}{\theta_{\mathrm{ref}}}(\theta - \theta_{\mathrm{ref}}), \tag{3}$$

where θ_{ref} is a reference potential temperature and g is the constant gravitational acceleration. The subfilter-scale momentum τ_{ij} and buoyancy flux B_j are parameterized using a subfilter-scale (SFS) turbulent kinetic energy (TKE) scheme (Deardorff, 1980). In Heus et al. (2010), the prognostic equation for SFS-TKE e with a canopy-drag force on SGS motions is (F_ε as explained in Section 2.2),

$$\frac{\partial e^{1/2}}{\partial t} + \tilde{u}_j\frac{\partial e^{1/2}}{\partial x_j} = \frac{1}{2e^{1/2}}\left[K_{\mathrm{m}}\left(\frac{\partial \tilde{u}_j}{\partial x_i} + \frac{\partial \tilde{u}_i}{\partial x_j}\right)\frac{\partial \tilde{u}_i}{\partial x_j} - K_{\mathrm{h}}\frac{\partial \tilde{b}}{\partial z}\right] + \frac{\partial}{\partial x_j}\left(2K_{\mathrm{m}}\frac{\partial e^{1/2}}{\partial x_j}\right) - \varepsilon - F_\varepsilon, \tag{4}$$

The first right-hand-side term contains SFS shear production and the buoyancy term. K_{m} and K_{h} are the turbulent eddy viscosities/diffusivities that vary spatially as a function of the SFS-TKE e (Deardorff, 1980). The SFS diffusion is the second right-hand-side term. The dissipation ϵ is parameterized in terms of e and a characteristic mixing length scale λ. Here we use a modified formulation of mixing length scale accounting for the near-surface effects (Dai et al., 2021).

2.2. Canopy physics

The sink and source terms induced by canopy elements arise as a result of the implicit filtering associated with discretizing the equations on a grid. In Eqs. (1), (2), (4), F_d, S_b, and F_ε represent the forcing and source terms attributable to the presence of the canopy (see Fig. 1). On grids without a tree, these terms equal zero. Within the canopy, the flow feels canopy influences through a combination of pressure drag and viscous drag F_d, through enhanced dissipation F_ε associated with the fine-scale boundary-layers forming on the individual canopy elements, and through buoyancy forces associated with leaf–air temperature differences S_b. Our study follows the parameterization of F_d and F_ε in Patton et al. (2016) (Fig. 1). The buoyancy force in the canopy model is incorporated with an air–plant–tissue heat exchange model, which was tested previously for this orchard (Boekee et al., 2023). This model calculates the plant-tissue temperature T_{p}, which results from the

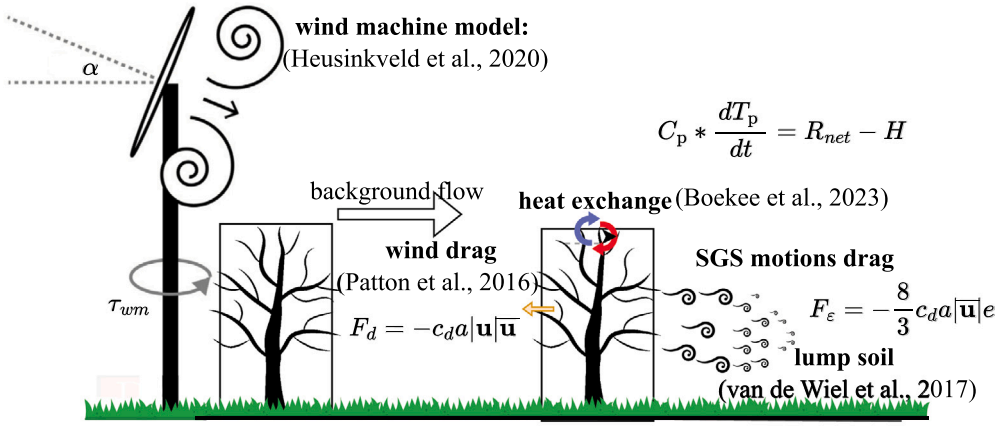

Fig. 1. The map illustrates physic modules integrated in the LES: the canopy model, the air–plant–tissue heat exchange model, the wind machine model, and the lump soil model. The setting of the grid where these parameterizations are applied are detailed in Section 3.

net effect of radiative cooling R_{net} and turbulent warming H (forced convection/advection by the WM),

$$C_{\text{p}} \frac{dT_{\text{p}}}{dt} = R_{net} - H, \tag{5}$$

where C_{p} is the plant-tissue heat capacity. R_{net} is calculated based on the Stefan–Boltzmann law, taking into account the temperatures of the sky, ground surface, and plants. The turbulent heat flux H between the leaves and the air in contact with them equals to,

$$H = \frac{\rho c_p (T_p - T_a)}{r_b}, \tag{6}$$

where ρ, c_p, T_a are the air density, heat capacity and temperature, respectively. r_b is the tissue boundary layer resistance for heat, which depends on the local Nusselt number, via the so-called 'air-refreshment velocity' (see Boekee et al. 2023). This velocity scale combines the effects from both free and forced convection (Schuepp, 1993). Based on the energy conservation within one grid-cell, the sensible heat source terms of the plant tissues H (W m^{-2}) and the air S_b (m s^{-3}) are related following,

$$S_b = \frac{g}{\theta_{\text{ref}}} \frac{Ha}{\rho c_p} \tag{7}$$

where a (m^2 m^{-3}) is the plant area density (PAD). The heat exchange model is designed to include different types of plant tissues. In this study, we developed and tested it specifically for leaf temperature prediction. Other plant tissues, such as flowers or woody crops, can be included by adjusting the heat capacity of the plant tissues (Boekee et al., 2023).

2.3. Wind machine parameterization

This section succinctly describes the wind machine parameterization detailed in Heusinkveld et al. (2020). The WM is idealized as an actuator disk. At each numerical time-integration step, we assume uniform distribution of momentum injected by the rapidly rotating blades across the disk. In the context of this study, which focuses on quantifying warming effects on plant tissues, detailed modeling of blade rotation effects is overly complex and computationally expensive. For future studies, it might be worthwhile to explore the impact of the blade characteristics using an actuator line model, similar to those used in wind turbine studies (e.g., Troldborg et al., 2007; Martinez et al., 2012). Additionally, the drag influence of the tower is considered to be negligible and is not included in the simulation.

The momentum forcing U_M injected at the exit of the numerical disk is calculated based on the work–energy principle: the power of the WM (P) is used to increase the kinetic energy of the air, which leads to an increased "exit velocity". From the appendix B1 of Heusinkveld et al. (2020), assuming a zero entrance velocity, the momentum forcing U_M is approximated as,

$$U_M = \hat{\boldsymbol{n}} \left(\frac{3Pl}{m} \right)^{1/3} \tag{8}$$

where $\hat{\boldsymbol{n}}$ is a unit vector normal to the numerical disk. m is the air mass and l is the disk thickness. Note that we do not explicitly model the thermodynamic effect of the engine heat that escapes due to motor inefficiency (Heusinkveld et al., 2020). However, in reality, this factor is observed to influence the temperature field locally (see Fig. 6). We intend to include only the most prominent physical mechanisms to simulate air mixing effects of the WM and avoid confounding effects. The height of the numerical disk is h_{wm}. The disk rotates with a prescribed rotation period per cycle (τ_{wm}) and it tilts slightly downward at an angle (α) of 8 degrees. The drag effect of the tower is ignored in the simulation.

2.4. The land-surface model

The coupling between the atmosphere and land surface is realized using a simplified surface-energy balance (van Hooft et al., 2019). This model calculates the sensible heat flux at the ground surface through the balance with net radiation and ground heat flux. The net radiation Q_s can be prescribed with a function during the course of simulations (e.g., a characteristic diurnal pattern as in van Hooft et al. 2019). During our short simulation period, we prescribe Q_s as a constant. The ground buoyancy flux G is parameterized using a lumped parameter model (Van de Wiel et al., 2017),

$$G = \Lambda (b_{\text{surf}} - b_{\text{soil}}), \tag{9}$$

where Λ denotes the lumped parameter, representing the feedback between the characteristic soil temperature b_{soil} and ground-surface temperature b_{surf}, expressed using their buoyancy equivalents (Eq. (3)). The soil is simplified as a homogeneous layer with a constant temperature. The interaction between the land surface and machine-induced air mixing plays a crucial role. Before the WM operation, b_{surf} is lower than b_{soil}, resulting in a positive ground heat flux for the surface layer. During the WM operation, the ground heat flux is reversed as the surface layer is warmed by the WM mixing effects. Normally, b_{surf} is determined using a Monin–Obukhov boundary condition. However, this approach results in extremely low values of b_{surf} in the presence of strong surface temperature gradients that occur during the WM operation. Moreover, Monin–Obukhov boundary conditions are often not well-defined within the canopy layer. Therefore, a simplified approach

is employed: when the jet passes over the surface (indicated by a surface friction velocity exceeding 0.01 m/s), the boundary condition is set to the temperature at the first grid level. If not, the boundary condition is adjusted to 90% of the temperature at the first grid level. Note that this land surface model is a simplification of the more complex reality. Such a simplification is chosen to balance the model complexity and physical realism. While this simplified approach captures essential dynamics (see Section 4.1), it is possible to incorporate more detailed models, such as a multi-layer soil scheme and/or a grass heat transfer model (van der Linden et al., 2022).

3. Simulation settings

The integrated model simulates the scenario from May 7, 2021 (Dai et al., 2023), where quasi-3D temperature responses to WM operation were measured in a pear orchard (Fig. 2c). The simulation includes a neutral spin-up period (200 min) followed by a period of surface cooling (50 min). The relatively long spin-up period is necessary to ensure the model reaches observed initial condition and the turbulence development under a very stable condition. The cooling phase begins with a 10-minute window without WM operation, followed by a 40-minute window with WM operation, featuring 8 rotation cycles, each lasting around 5 min. The computational domain spans (2048, 2048, 2048)-m in (x, y, z) directions. x and y are horizontal streamwise and cross-stream directions, respectively. z represents the height from the surface (vertical axis).

Using the AMR method, the refinement levels vary from 5 to 11, corresponding to grid-element sizes of 64 m and 1 m, respectively. Cartesian grids dynamically refine or coarsen between these numbers of levels based on a specified refinement criterion. Error thresholds for wind velocities and buoyancy (in temperature value) are set at 0.3 m/s and 0.35 K, respectively. A minimum grid size of 1 m is set near the canopy and disk to ensure fully resolved features. Fig. 2a illustrates the grid structure on an x–z slice at $y = 1024$ m, mirroring the layout of the experimental pear orchard (see Fig. 2c) described in Dai et al. (2023). In this orchard, the height of trees h and spacing of tree rows r_{tr} are 3 m. The orientation of tree lanes to the background wind during the experiment is roughly 45° to the east. To configure such a layout in the simulation, the numerical tree lanes are implemented with a conditional function $TL(x, y, z)$,

$$TL(x,y,z) = \begin{cases} 1, & \text{mod}\,(|x-y|,4) = 0 \text{ and } z \le h \\ 0, & \text{otherwise} \end{cases} \tag{10}$$

where mod is a modulus operator. Canopy effects are applied to the *tree-grids* where $TL > 0$. With 1 m grid size near the canopy, r_{tr} equals 2.82 m (Fig. 2b). The canopy is vertically resolved by 3 grid points with a constant PAD profile a ($\mathrm{m^{-2}\ m^{-3}}$) of 1.20 over height. The drag coefficient c_d quantifies the efficiency of momentum absorption by canopy elements whose varies slightly with wind speed (Patton and Finnigan, 2013). Brunet et al. (1994) address the height-dependency of c_d for a wheat-model in a wind tunnel. Furthermore, even assuming c_d is constant, its value is reported to vary across different settings and applications (see Table 1). For simplicity, c_d is set as a constant of 0.20 in this study. The appropriate parameterization of c_d for the current application requires thorough experimental design and numerical investigation, which is beyond the scope of this study. The constant value of PAD and c_d is an empirical setting based on trial and error of 2D simulations. We checked if the spin-up temperature profiles reach a quasi-steady state and align with observations (results not shown). Then, we further tested the 3D simulation results against the field data.

Leaf temperatures are modeled at the *tree-grids* by solving Eq. (5). The simulated leaf temperatures will be compared with measurements from Boekee et al. (2023). The air–plant–tissue heat exchange model allows for other tissue types by modifying the characteristics of the plant tissue. The parameters for three tissue types including the leaf can be found in Boekee et al. (2023). The leaf temperature profile is initialized as a constant temperature of $T_p = 6$ °C within the canopy.

Table 1
This table aims to show a range of drag coefficient c_d values from some applications, rather than to explain the reasons for these specific values.

Studies	Application	Drag coefficients
Raupach et al. (1986)	vertical aluminum strips in a wind tunnel	1.6
Dwyer et al. (1997)	following (Shaw et al., 1988)	0.15
Katul et al. (2004)	eight terrestrial plant types	0.10–0.30
Finnigan et al. (2009)	following (Brunet et al., 1994)	0.47
Chahine et al. (2014)	a vineyard	0.20
Torkelson et al. (2022)	a model of the vineyard canopy in a wind-tunnel	0.50
The present study	a pear orchard	0.20

The numerical disk description mimics the real outdoor WM (Dai et al., 2023) and has the dimensions of a 6 m diameter located at 10.5 m (hub) height. The disk is placed at location of (500, 1024, 10.5)-m in the (x, y, z) directions (Fig. 2a). The tilting angle α is 8°. The rotational period τ_{wm} is found to be 288 s based on numerical testing, which is slightly shorter than the user-specified setting (300 s). The WM-power to the air mass ratio P/m is set as 3000 $\mathrm{m^2\ s^{-3}}$ based on a technical report from the manufacturer.

Winds were very light during the experiment. The pressure gradient force in the direction of the mean wind is estimated based on the surface friction (Eq. 2 from Van de Wiel et al. (2003)). The measured friction velocity at the canopy top is 0.0335 $\mathrm{m\ s^{-1}}$. The calculated pressure gradient force is in the order of $\mathcal{O}(10^{-7})$ to $\mathcal{O}(10^{-6})$ $\mathrm{m\ s^{-2}}$. This value is extremely small and results are not sensitive to this value based on numerical testing. The bulk Richardson number is around 3, which suggests a very stable condition. The turbulent Reynolds number is in the order of $\mathcal{O}(10^6)$. The initial conditions of wind and air temperature are based on the fifth generation of global climate reanalysis data, ERA5 (Hersbach et al., 2023). A constant air temperature of 9.5 °C is initially set from the surface up to 100 m height and then linearly increasing with a constant rate of 3 °C $\mathrm{km^{-1}}$. The initial wind profile u is a function of the height z,

$$u = \begin{cases} 0.25 \ln\left(z/z_{0\mathrm{m}}\right)\ \mathrm{m\ s^{-1}}, & z < 300 \text{ m} \\ (1.6 + 0.01(z-300))\ \mathrm{m\ s^{-1}}, & 300 \text{ m} \le z < 1024 \text{ m} \\ 9\ \mathrm{m\ s^{-1}}, & 1024 \text{ m} \le z < 2024 \text{ m} \end{cases} \tag{11}$$

where the aerodynamic roughness length $z_{0\mathrm{m}}$ equals 0.1 m. The initial profile of SGS-TKE (e) is set as constant 5×10^{-5} $\mathrm{m^2\ s^{-2}}$. In the surface layer, the characteristic lumped parameter Λ is set as 0.0035 $\mathrm{m\ s^{-1}}$, in equivalent to 4.6 $\mathrm{W\ m^{-2}\ K^{-1}}$, which is an average value during the night time condition based on data obtained at Cabauw (van Hooft et al., 2019). A summary of the parameters used in this study is presented in Table 2.

To prevent the formation of gravity waves at the top boundary, a sponge layer is applied in the upper half of the domain (Klemp and Lilly, 1978). In our simulation, dealing with the complex effects of tree lanes and the WM requires careful consideration of lateral boundary conditions. To dampen wave effects by the WM, a buffer/absorbing layer is applied near lateral boundaries. In this layer, the standard practice is to nudge the flow fields towards a predefined solution. However, such fixed and homogeneous solution conflicts with the heterogeneous cooling effects from tree lanes and the surface. Another alternative is radiation boundary conditions, which allows wave movement out of the simulation domain. In our implementation, this also proved challenging because the vertical velocity is quite sensitive to the presence of irregular tree lanes. To overcome this issue, we set periodic lateral boundary conditions in a large-size domain. This setting means that even though the focus of this work is on a single orchard, the simulation actually reflects flow over an infinitely repeating set of orchards. We show in Appendix A that the wave effect has diminished below our specified

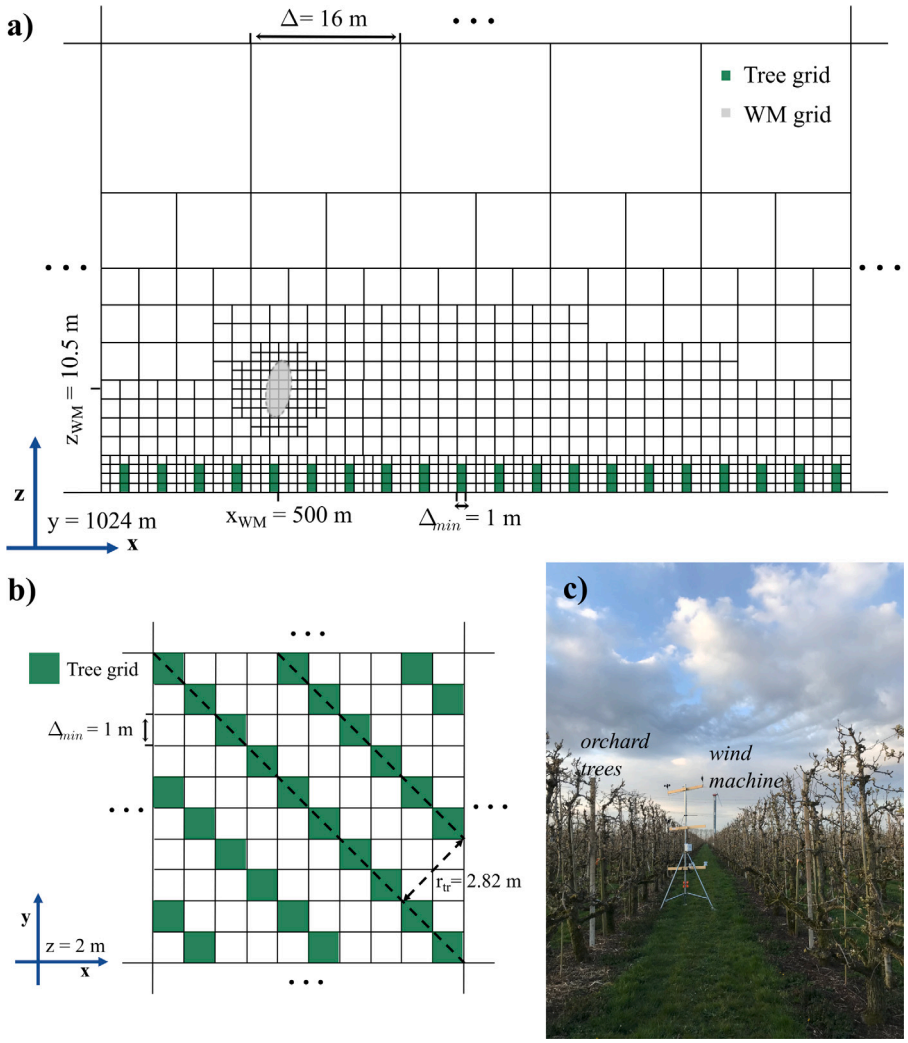

Fig. 2. The illustration shows a sample grid structure on two planes: the x–z plane at y = 1024 m (panel a) and the x–y plane at z = 2 m (panel b). The grid structures in panels a and b are from specific sections, visualized at different scales for clarity. In panel a, the *WM-grids* are shown when the numerical disk aligns with the x direction. The resolved *WM-grids* adapt with the WM's rotation. Additionally, panel c shows the experimental site, including the wind machine, tree lanes and weather station.

Table 2
A summary of the parameters used in this study. The values inside of brackets are their buoyancy equivalents.

Symbols	Variables	Values
C_p	leaf heat capacity	2E6 J m^{-3} K^{-1}
c_d	drag coefficient	0.20
a	plant area index	1.2 m^2 m^{-3}
c_p	air heat capacity	1005 J kg^{-1} K^{-1}
P/m	the power of the WM per air mass	3000 m^2 s^{-3}
l	the thickness of WM disk	0.3 m
h_{wm}	height of the WM	10.5 m
U_M	WM momentum forcing	13.92 m s^{-1}
α	tilting angle of the WM	8°
Q_s	net radiation at the ground surface	−7.2 W m^{-2} (−0.00024 m^2 s^{-3})
Λ	the characteristic lumped parameter	4.0 W m^{-2} K^{-1} (0.0035 m s^{-1})
b_{soil}	the lump soil temperature	2.7 °C (0.1 m s^{-2})

refinement criterion before exiting the downwind domain boundary and re-entering the upwind boundary. For future studies, more dynamic and flexible technique of lateral boundary conditions by Araya et al. (2011), Munters et al. (2016) can be employed for the application of multiple-WMs.

The simulation required 75.5 wall-clock hours utilizing 1024 computer cores. The number of numerical grid cells is around 4.4E7, which is around 0.5% of the total 2048^3 grid points that would have been used with uniform Cartesian grids. After the spin-up period, 3D snapshots of wind velocities (u_1, u_2, u_3), buoyancy term (b), and leaf temperatures (T_p) on adaptive grids are dumped at a logging interval of 4 s (Fig. 2ab). The average size of each snapshot is approximately 2.6 GB, totaling 1.95 TB of output data. For ease of comparison with field observations, output fields from grid cells larger than the minimum grid size of 1 m are interpolated onto regular Cartesian grids with a uniform grid size of 1 m. The simulation data, near a 9 m tower located 30 m downstream, are logged at a frequency of 1 s.

4. Results and discussion

Here, we focus on the comparison between the simulation and measurements, and the physical interpretations of the measurements are detailed in Dai et al. (2023).

4.1. Comparison with experimental data

Time-averaged vertical temperature profiles before and during the operation period along tower W1 are presented in Fig. 3. Before the WM operation, a strong temperature inversion forms just above the canopy

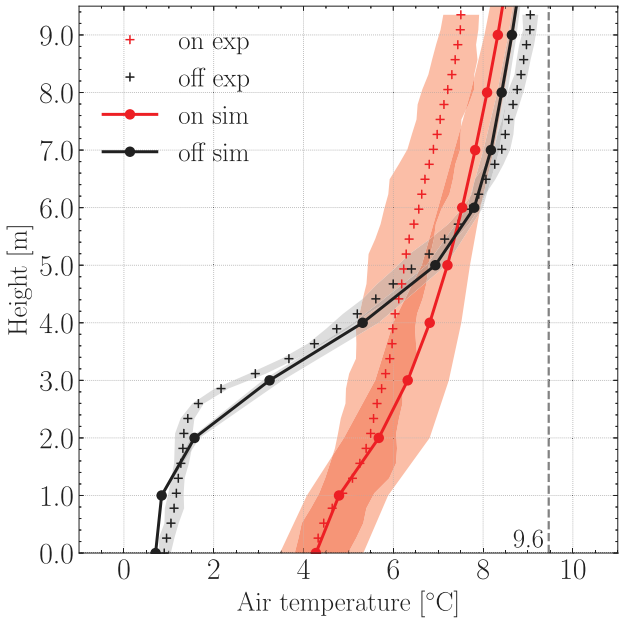

Fig. 3. Comparison of measured (plus markers) and modeled (solid lines with circle markers) time-averaged vertical temperature profiles during the on (red) and off (black) mode at tower W1. The standard deviation of the air temperatures is included with shaded contours.

as a result of the longwave radiative cooling. Within the canopy, the temperature profile is nearly neutral. The canopy model simulates the temperature profile before WM operation well. During WM operation, air mixing caused by the WM erodes the temperature inversion. The model is capable of simulating the warming within the canopy, whereas temperatures above the canopy are slightly overestimated compared to observations. The discrepancy can be explained by the fact that in reality the WM had a start-up period of about 45 min, where it had two 'intermittent/irregular' cycles. During this period the system already cooled. However, the simulation excluded this non-stationary period (only regular cycles were considered), and therefore the additional cooling was not accounted for (Fig 6 of Dai et al. 2023).

Fig. 4 compares the measured (a) and modeled (b) time height plot of air temperatures at tower W1. Panel c shows observed and modeled temperature time series at heights of 1 m and 9 m. During WM operation, the warm plumes periodically penetrate from the top into the canopy. As a result, the canopy airspace temperatures briefly rise and the temperatures start to drop after warm plumes pass by. Simulation results capture the periodic warming–cooling pattern and magnitude well. The model slightly overestimates air temperatures at 9 m height. Similar to Fig. 3, this is likely due to the exclusion of the start-up period from the simulation. Before WM operation, temperature signals show canopy-induced wave-like fluctuations near the canopy top, similar to the observations in a forest canopy (Lee and Barr, 1998). These fluctuations are less pronounced in the measurements, possibly due to the higher logging frequency in simulations (1 s) compared to the measurements (10 s).

Fig. 5 displays measured (a) and simulated (b) time series of air and leaf temperatures over 8 rotation cycles. The model captures the dynamics of air and leaf temperatures well, specifically the periodic warming–cooling pattern and air–leaf temperature magnitude. Prior to operation, simulated leaf–air temperature differences are around 0.5 °C larger than measured differences (around 1 °C). This could be attributed to the leaf energy budget representation (e.g., net radiation), which is highly simplified. Similar overestimation of leaf–air temperature differences was observed after the warming plumes pass by. During the rotation cycle, as the jets pass by, leaf temperatures closely follow

Table 3
Descriptive statistics of observed and simulated wind speed M (m s^{-1}) during on and off modes at tower W1. The frequency of the measured wind speed is 10 hz and it is sampled in the same frequency as the simulation output 1 s.

	Measurement (m s^{-1})	Simulation (m s^{-1})
$\overline{M_{off}}$	0.44	0.47
$\sigma_{M_{off}}$	0.06	0.04
max (M_{off})	0.60	0.58
min (M_{off})	0.30	0.38
$\overline{M_{on}}$	1.08	0.88
$\sigma_{M_{on}}$	1.01	0.81
max (M_{on})	7.76	7.99
min (M_{on})	0.54	0.11

the air temperatures, indicating a strong coupling due to effective heat exchange, which was also reported in the observational study of Boekee et al. (2023). Just before the arrival of the jet, a relatively larger difference between air and leaf temperatures is observed in both the simulation and measurement. This is due to radiative cooling by the leaf.

Time-averaged air temperature changes before and during operation over a horizontal plane at 2 m height from measurements (a) and simulation (b) are shown in Fig. 6. Overall, the simulated temperature change agrees remarkably with measurements in terms of the magnitude, coverage and shape. In the area of warming larger than 4 °C, the warming shape is slightly different from the measurements and the magnitude of simulated warming is larger than measured warming. Additionally, both simulated and observed warming plumes are observed to drift downstream relative to the WM (see instantaneous movies of the warming plumes in supplementary material). This results from the advection of the plumes by the wind similar to drifts reported in other studies (e.g., Beyá-Marshall et al., 2019; Heusinkveld et al., 2020; Dai et al., 2023). In measurements (panel a), the white spot near the WM indicates the heat emission by the engine. This aspect is not included in our simulation for simplicity and to prevent overlapping of physical effects.

Table 3 summarizes the statistics of the total wind speed M at tower W1 during on and off modes. Overall, there is a good agreement between the measurements and simulation, except for the underestimated minimum wind speed during operation. Fig. 7 compares phase-averaged wind velocities over 8 rotation cycles between the simulation and measurements. A similar underestimation of minimum wind speed just before operation is observed, likely due to the more idealized nature of the simulation compared to physical reality. When the jet passes by, and after it has passed the tower, the simulated wind speed aligns closely with the measurements.

4.2. Simulated vertical, streamwise and cross-stream profiles

Fig. 3 shows that simulated temperature profiles agree with measurements at tower W1. To understand the WM influence across the field, wind and temperature profiles are binned by their radial distance from the WM and profiles within each bin are averaged. In Fig. 8, radially averaged wind (a) and air temperature (b) vertical profiles reveal two distinct mixing zones influenced by the WM's operation: the near-jet and far-jet mixing zones. The near-jet mixing zone, characterized by high wind velocities up to 9 m s^{-1} at 1 m from the WM at hub height, extends up to about 20 m from the WM location. The range of the near-jet mixing zone is defined by regions where the wind profile exhibits a clear jet-like shape. Wind velocities decrease rapidly with increasing radial distance from the WM. Similarly, air temperatures adjacent to the WM at lower heights exhibit increased warming because of the direct jet-mixing effects. This effect is most pronounced around 20 m from the machine (the black dashed profile). Interestingly, the temperature profile near the WM (red dashed line) shows a decrease at hub height relative to areas farther from the WM. This suggests that maximum

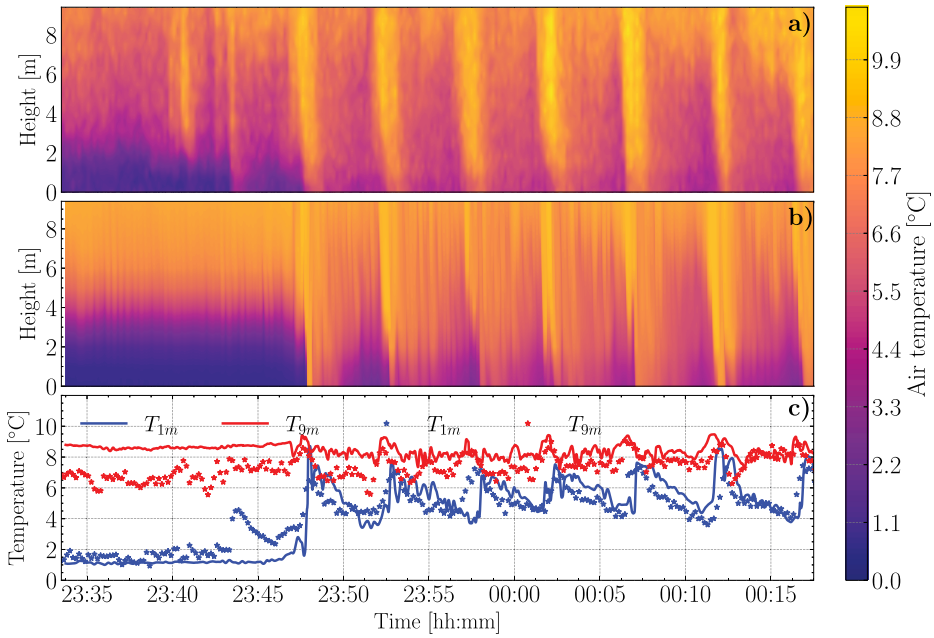

Fig. 4. Observed (a) and modeled (b) time height plot of air temperatures at tower W1. Panel c shows time series of 1 m (blue) and 9 m (red) air temperatures from the simulation (solid lines) and measurements (star markers).

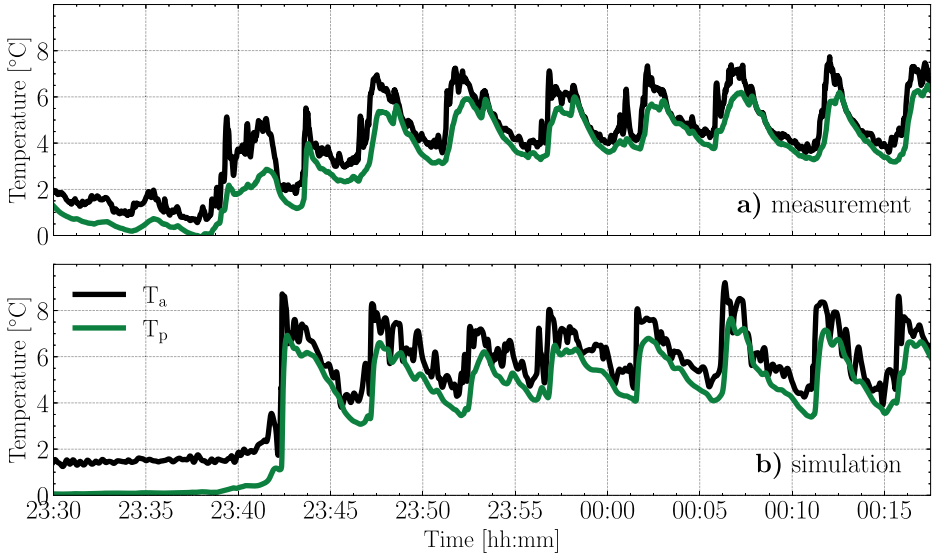

Fig. 5. Observed (a) and modeled (b) time series of air (T_a in black) and leaf (T_p in green) temperatures over 8 rotation cycles.

warming near the surface at around 20 m from the WM is caused by downward mixing of warmer above-canopy air at the hub height of the WM. The air temperature at the WM location is not warmer than at 21 m due to the 'overblowing effect' of the WM. However, we note here that caution should be taken with a strict 1-D 'ballistic view', because lateral advection from earlier warmed sections is significant also close to the WM (Fig. 6).

The air mixing zone beyond 20 m away from the WM is labeled as the far-jet mixing zone, featuring contrasting changes in wind and temperature profiles. This sharp transition of wind profiles beyond the near-jet mixing zone shows the strongly reduced influence of mechanical propeller rotation. This is not only the result of canopy drag, but also of momentum conservation, as with increasing radius more air is entrained into the jets. Notably, in the absence of direct jet mixing and with a mean wind velocity of 0.2 m s^{-1} within the canopy, the air temperature warming remains and decreases gradually with increasing distance from the WM. This sustained warming is likely due to the advected warming air induced by the jets, which is demonstrated in the supplementary material. The upper bounds of the far-jet mixing zone are 150 m upstream and 550 m downstream, respectively (discussed in Fig. 9). For better interpretations and understanding, the mixing zones are labeled as direct-jet and far-jet mixing. In future studies, it is recommended to explore the quantitative definition of mixing zones and the relationship to the WM thrust, the atmospheric stability and canopy characteristics.

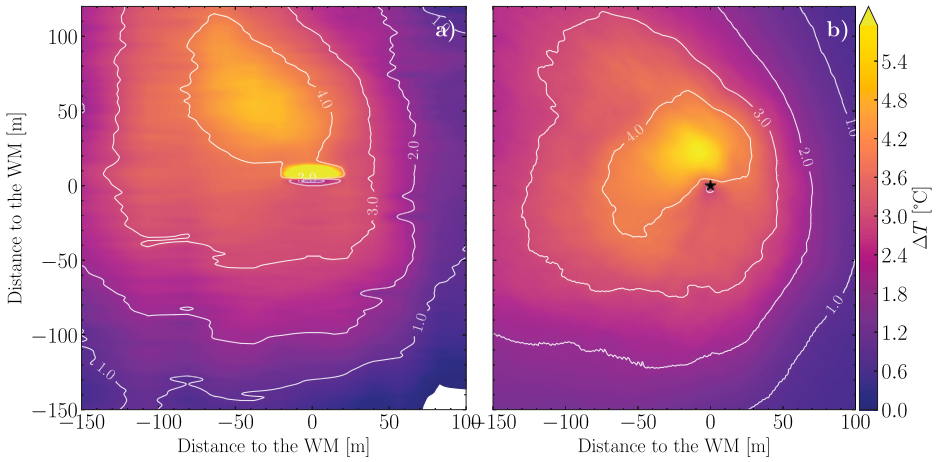

Fig. 6. Comparison of measured (a) and modeled (b) time-averaged air temperature changes over a horizontal plane at 2 m height. The slice from simulation is rotated 45° to align with the measurements. The WM is located at (0, 0). The heat plume emitted by the engine is only visible in the measurements.

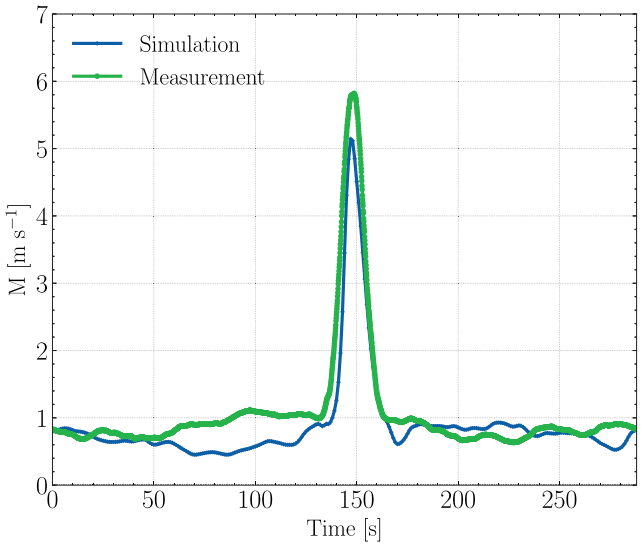

Fig. 7. Comparison of measured and modeled phase-averaged wind velocities over 8 rotation cycles.

To further investigate the range of warming in horizontal directions, we space–time-average air and leaf temperature profiles along *streamwise* (x) and *cross-stream* (y) directions. In Fig. 9a, in the *streamwise* direction, the temperatures within the canopy ($z \leq 3$ m) are first averaged over y-z slices and then averaged for both off and on periods. During the operation, enhanced warming of the air and leaves is observed to extend further downstream than upstream, with the maximum warming occurring at around 20 m downwind. Considering the error threshold for the air temperature being 0.35 K, we estimate the warming ranges between roughly 150 m upstream and 550 m downstream. This asymmetry in warming is caused by the weak background wind (0.2 m s^{-1} within the canopy), which hinders or helps the development of the warming plume upstream or downstream, respectively. The same phenomenon is reported in Heusinkveld et al. (2020), Dai et al. (2023). It is noteworthy that the simulated warming range 550 m downstream is larger than the limited measurement range of 130 m in Dai et al. (2023). In the *cross-stream* direction (Fig. 9b), x–y slices are averaged. The cross-stream picture is much more symmetrical, because the direct influence of the background wind is limited. Warming ranges for both air and leaves extend to approximately 250 m on each side.

Near the WM, leaf temperatures closely follow air temperatures in both *streamwise* and *cross-stream* directions. In contrast, at greater distances from the WM, the difference between leaf and air temperature is about 1 degree. This variation in distances is linked to the WM-induced air warming and air–leaf heat exchange dynamics (Fig. 9bd). Near the WM, the turbulent heat flux H increases (negatively) due to elevated air temperature and wind speed, thus raising the leaf temperature. Even though radiative cooling intensifies with leaf warming, turbulent warming is predominant except where leaf and air temperatures are nearly equal. This is because H linearly relates to the temperature difference between the leaf and air. At a further distance from the WM, both air and leaf temperatures are approximately 0.35 °C higher during operation than in the off period, which seems inconsistent with the negative leaf energy budget. The overestimated warming is likely due to the machine-induced warming circulated within the periodic domain, but its magnitude is relatively minor compared to the error threshold of 0.35 °C.

4.3. Simulated phase-averaged streamwise sections

Two instances of phase-averaged air temperature (in contours) and wind (in arrows) sections are shown in Fig. 10 to illustrate the mixing dynamics between warm plumes and ambient wind. The interactions are shown in opposing (a) and aligning (b) directions. These sections are taken from the midpoint of the *cross-stream* direction. In panel a, where the jet flows against the background wind, wind arrows depict a convergence pattern upwind of the WM. This is due to the collision between the decelerating jet and the background airflow. This agrees with the second warming plume measured in Dai et al. (2023). When the jet flows with the background wind (panel b), warming plumes travel further, creating wave-like patterns downstream. As a result of the background wind advection, downstream warming extends to a greater distance than the warming upstream (Figs. 6 and 9). Instantaneous movies of the warming plumes in supplementary material show the dynamic interactions between the jet and the background wind.

5. Conclusion

The present study implements an integrated model in LES to quantify the warming effects of WM operation on plant tissues. For the first time, this model integrated in LES incorporates an air-vegetation energy exchange model and a highly dynamic driver of atmospheric disturbance (the wind machine). We compare simulation results with quasi-3D temperature measurements based on 9 km of fiber optic

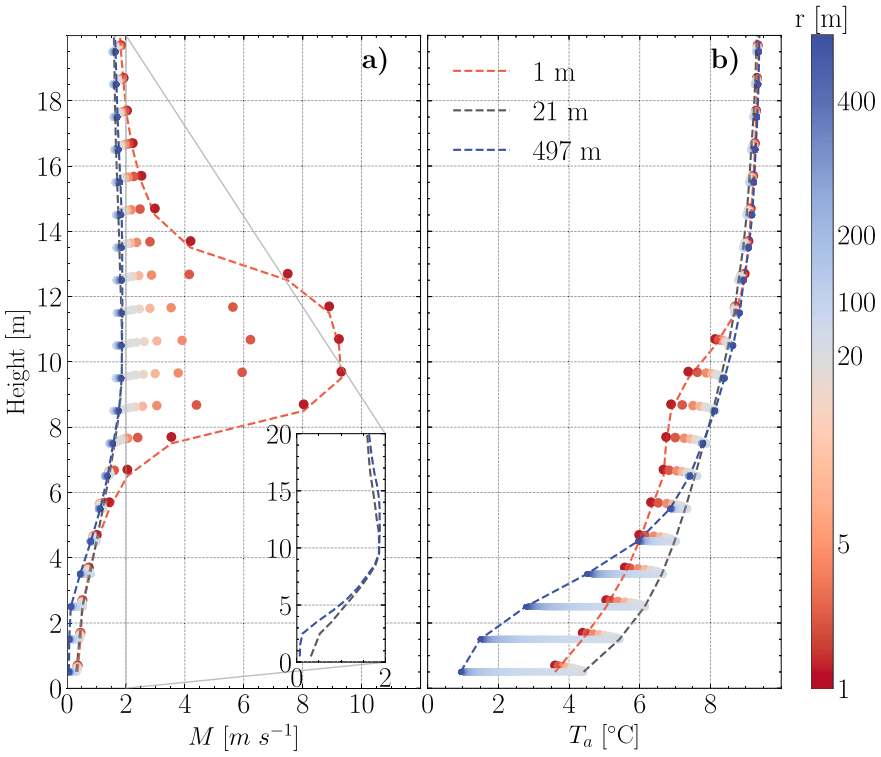

Fig. 8. Distribution of vertical profiles of wind velocity M (a) and air temperature T_a (b) with increasing distance r [m] from the wind machine. The distance is marked by the color bar. Three profiles at 1, 21 and 499 m away from wind machine are lined. The dots of profile from 1 to 21 m are artificially elevated by 1 cm to avoid overlapping. A zoom-in window in panel a illustrates the canopy-influenced wind profile (blue dashed line) at further distance and the differences to the profile at 21 m (black dashed line).

cables over a 6.75 ha orchard (Dai et al., 2023). Our integrated model can reproduce the complex mixing and warming effects of the WM operation observed in the field.

Based on the numerical simulation,

- during WM operation, two distinct mixing zones are present: near-jet and far-jet mixing zones. The near-jet mixing zone extends up to about 20 m from the WM location, a length of 3–4 rotor diameters. This zone is predominantly influenced by direct mixing of the jet. We found that the maximum warming near the surface at around 20 m from the WM is caused by downward mechanical mixing of warmer above-canopy air at the hub height of the WM. In the absence of direct jet mixing, the air warming decreases gradually with distance from the WM in the far-jet mixing zone. This sustained warming is likely due to the advected warming air induced by the jets.
- The background wind despite being light (0.2 m s^{-1}) causes a strong difference in the warming of air and leaves upstream and downstream of the WM. When jets flow against the background wind, the wind depicts a convergence pattern. When jets flow along the background wind, warming plumes travel further, creating wave-like patterns downstream. As a result, the downstream warming range extends much further than the upstream range (550 m compared to 150 m). In cross-stream direction, both warming ranges for air and leaves extend to approximately 250 m on each side.
- Within these warming ranges, leaf temperatures closely follow air temperatures due to strong turbulent heat exchanges. Outside the warming zone, radiative cooling prevails, returning the leaf–air temperature difference to approximately 1 degree.

While our integrated model is able to reproduce air mixing effects observed in an experiment (Dai et al., 2023), there is potential for further improvement of the model. Before the WM operation, simulated leaf–air temperature differences are around 0.5 °C larger than measured differences (around 1 °C). We attribute this to the leaf energy budget representation, which is highly simplified. Currently, the leaf energy balance model calculates the radiation budget within canopy based on a Stefan–Boltzmann law. For future studies, it is recommended to incorporate the scattering and reflection of radiation using a canopy radiation model (Patton et al., 2016; Guenther et al., 2006).

Furthermore, it is realized that our model is only compared to a single observational case, which may limit the generality of the outcome. In future studies, we aim to conduct more field experiments for model development. The development of the fiber-optic sensing technique (van Ramshorst et al., 2020; Freundorfer et al., 2021) enables obtaining temperature and wind speed measurements at high resolutions and over large spatial areas. Additionally, various types and operations of wind machines should be investigated. Our study finds that the warming plumes travel further with the help of the background wind. This may suggest that other WM operational modes (e.g., sweeping half circles along the wind) may perhaps be equally or more efficient. This needs to be investigated.

Overall we conclude that the model provides a useful surrogate of outdoor reality with respect to wind machine operation in orchards. As such, it can be used to explore various scenarios to further optimize the efficiency of WM operation under various conditions. For instance, we can investigate the warming effects concerning different WM designs with different rotor diameters and WM power levels. Apart from testing the 180° rotation of WMs, the combined warming effects of WMs and heaters can be numerically investigated. It enables possibilities for the development of anti-frost wind machines and new frost mitigation methods. Overall, this numerical study confirms that the WMs are able to significant change the local climate in orchards as to mitigate frost damage over several hectares. As such, numerical models such as presented here may help to improve understanding of machined-induced plant warming systems.

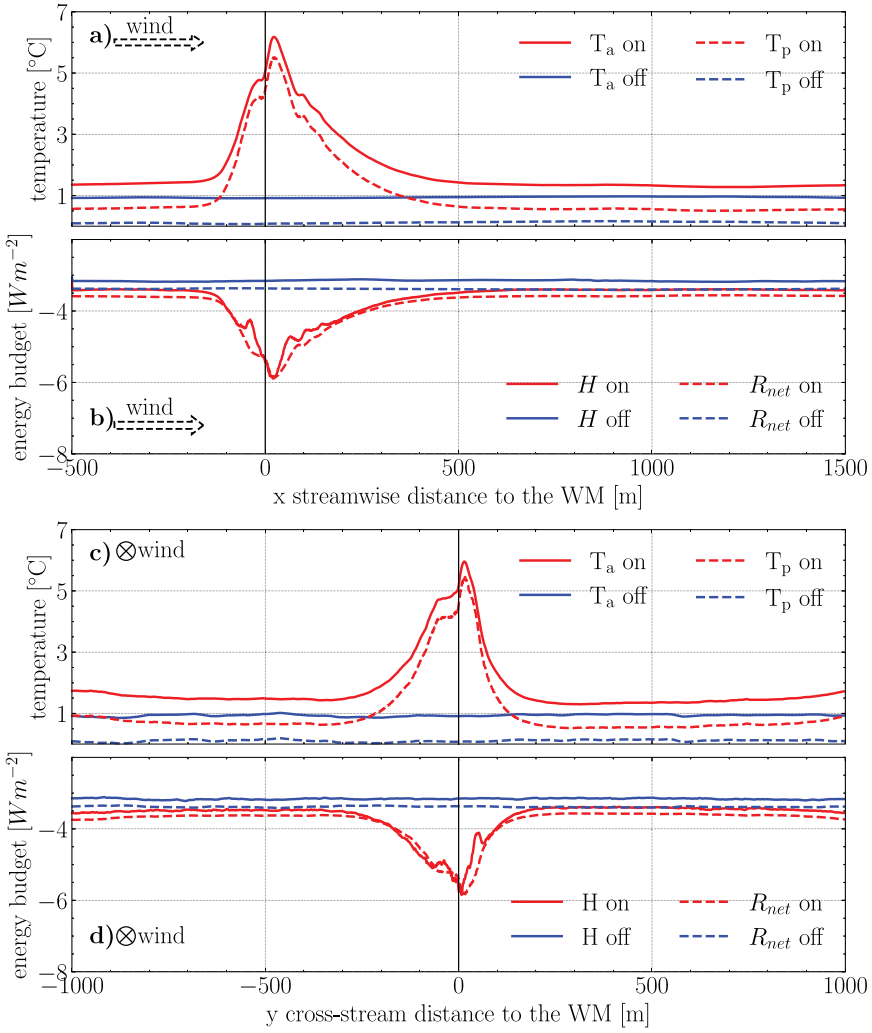

Fig. 9. The spatial-time-averaged air (T_a in solid lines) and leaf (T_p in dashed lines) temperature profiles along *streamwise* (**a** panel, z = 1024) and *cross-stream* (**c** panel, x = 500) directions. Averaged periods of on and off modes are represented by red and blue lines. The corresponding leaf energy budgets of the turbulent heat flux H and net radiative cooling R_{net} are shown in other two panels. The wind machine location (0, 0) in (x, y) direction is indicated with black solid lines.

CRediT authorship contribution statement

Yi Dai: Methodology, Modeling, Investigation, Visualization, Original manuscript writing & review & editing. **Antoon van Hooft:** Methodology, Validation, Supervision, Manuscript review. **Edward G. Patton:** Manuscript review, Validation, Methodology. **Judith Boekee:** Manuscript review, Methodology. **Steven van der Linden:** Manuscript review, Supervision. **Marie-Claire ten Veldhuis:** Manuscript review & editing, Supervision. **Bas J.H. van de Wiel:** Manuscript review & editing, Validation, Supervision, Conceptualization.

Declaration of competing interest

The authors declare that they have no known competing financial interests or personal relationships that could have appeared to influence the work reported in this paper.

Data and code availability

Upon acceptance of the manuscript, the model, analysis codes and processed data will be made publicly available on github.

Acknowledgments

The authors are grateful to Stephan de Roode, Pier Siebesma, Sukanta Basu and John Finnigan for fruitful discussion. We thank the Dutch Research Council NWO for the project funding (EN-WSS.2018.006). Simulations were carried out on supercomputers: (1) Delft-Blue operated by Delft High Performance Computing Centre (DHPC) and (2) Snellius, the Dutch National supercomputer hosted by SURF Cooperative.

Appendix A. Periodic boundary conditions in a large-size domain

In this appendix we demonstrate, using periodic boundaries, that the wave effects generated by the WM have little influence on the inflow boundary condition. Fig. A.11a presents the streamwise air temperature at 2 m height over the simulation period. After the WM starts operation, the air temperatures rise near the WM and the warming effect propagates downstream and upstream. Due to the background wind effect, the warming waves propagate further downstream than upstream. In panel b the time-averaged temperature profiles during the operation warms much close to the WM. At the boundaries of domain, these two profiles shows little influence of the WM mixing. This is also the case for an instantaneous temperature profile during the operation.

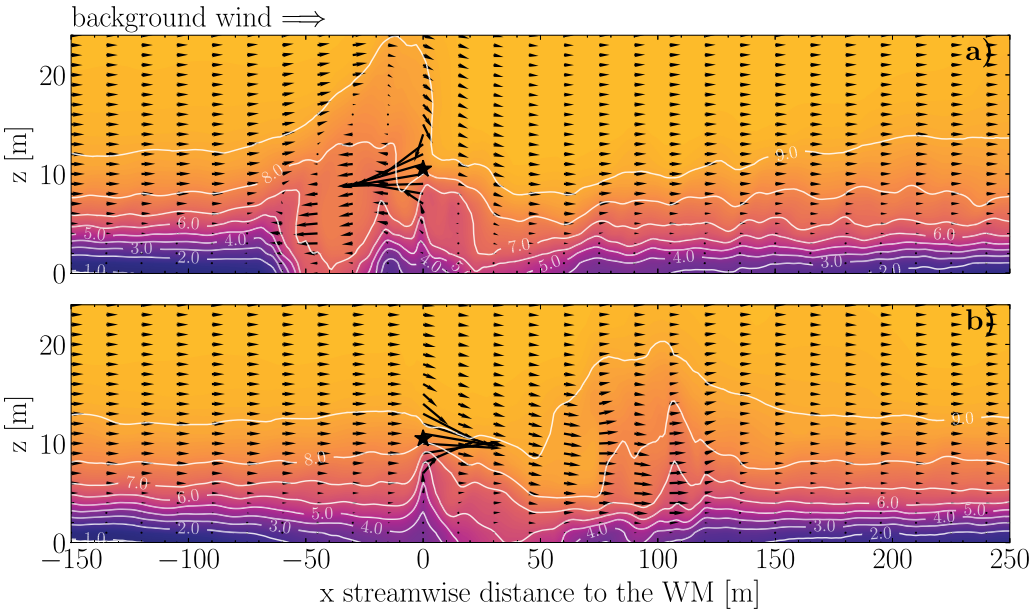

Fig. 10. Phase-averaged air temperatures (in contours) and wind (in arrows) along the *streamwise* section. The section is taken from the center of the *cross-stream* direction. Two instances are presented when the jet flows against (a) and aligned with (b) the background wind. In panel a, a convergence vortex structure develops upwind of the WM. The center location of the wind machine hub is marked with a black star.

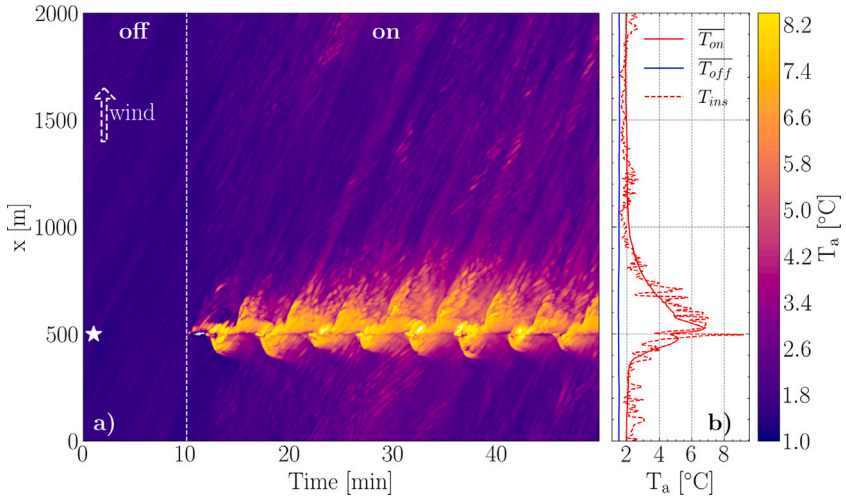

Fig. A.11. Panel a shows the distribution of streamwise air temperatures at a 2 m height during the off and on periods of the WM. These profiles are taken across the WM location. The starting time of the WM is marked by a white dashed line. The WM location is denoted by a white star and the direction of the background wind is indicated with a white dashed arrow. In panel b the air temperature profiles are time-averaged for off and on periods (T_{on} and T_{off}) and one instantaneous profile (T_{ins}) is plotted from the operation period.

Appendix B. Supplementary data

Supplementary material related to this article can be found online at https://doi.org/10.1016/j.agrformet.2024.110175.

References

Araya, G., Castillo, L., Meneveau, C., Jansen, K., 2011. A dynamic multi-scale approach for turbulent inflow boundary conditions in spatially developing flows. J. Fluid Mech. 670, 581–605. http://dx.doi.org/10.1017/S0022112010005616.

Battany, M.C., 2012. Vineyard frost protection with upward-blowing wind machines. Agricult. Forest Meterol. 157, 39–48. http://dx.doi.org/10.1016/j.agrformet.2012.01.009.

Beyá-Marshall, V., Herrera, J., Santibáñez, F., Fichet, T., 2019. Microclimate modification under the effect of stationary and portable wind machines. Agricult. Forest Meterol. 269, 351–363. http://dx.doi.org/10.1016/j.agrformet.2019.01.042.

Boekee, J., Dai, Y., Schilperoort, B., van de Wiel, B.J., ten Veldhuis, M.-C., 2023. Plant–atmosphere heat exchange during wind machine operation for frost protection. Agricult. Forest. Meterol. 330, 109312. http://dx.doi.org/10.1016/j.agrformet.2023.109312.

Brunet, Y., Finnigan, J., Raupach, M., 1994. A wind tunnel study of air flow in waving wheat: single-point velocity statistics. Bound.-Layer Meteorol. 70 (1–2), 95–132. http://dx.doi.org/10.1007/BF00712525.

Chahine, A., Dupont, S., Sinfort, C., Brunet, Y., 2014. Wind-flow dynamics over a vineyard. Bound.-Layer Meteorol. 151, 557–577. http://dx.doi.org/10.1007/s10546-013-9900-4.

Dai, Y., Basu, S., Maronga, B., de Roode, S.R., 2021. Addressing the grid-size sensitivity issue in large-eddy simulations of stable boundary layers. Bound.-Layer Meteorol. 178, 63–89. http://dx.doi.org/10.1007/s10546-020-00558-1.

Dai, Y., Boekee, J., Schilperoort, B., ten Veldhuis, M.-C., van de Wiel, B.J., 2023. Wind machines for frost damage mitigation: A quantitative 3D investigation based on observations. Agricult. Forest. Meterol. 338, 109522. http://dx.doi.org/10.1016/j.agrformet.2023.109522.

Deardorff, J.W., 1980. Stratocumulus-capped mixed layers derived from a three-dimensional model. Bound.-Layer Meteorol. 18, 495–527. http://dx.doi.org/10.1007/BF00119502.

Delft High Performance Computing Centre (DHPC), 2024. DelftBlue Supercomputer (Phase 2). https://www.tudelft.nl/dhpc/ark:/44463/DelftBluePhase2.

Dwyer, M.J., Patton, E.G., Shaw, R.H., 1997. Turbulent kinetic energy budgets from a large-eddy simulation of airflow above and within a forest canopy. Bound.-Layer Meteorol. 84, 23–43. http://dx.doi.org/10.1023/A:1000301303543.

Finnigan, J.J., Shaw, R.H., Patton, E.G., 2009. Turbulence structure above a vegetation canopy. J. Fluid Mech. 637, 387–424. http://dx.doi.org/10.1017/S0022112009990589.

Freundorfer, A., Lapo, K., Schneider, J., Thomas, C.K., 2021. Distributed sensing of wind direction using fiber-optic cables. J. Atmos. Ocean. Technol. 38 (10), 1871–1883. http://dx.doi.org/10.1175/JTECH-D-21-0019.1.

Frith, H., 1951. Frost protection in orchards using air from the temperature inversion layer. Aust. J. Agric. Res. 2 (1), 24–42.

Guenther, A., Karl, T., Harley, P., Wiedinmyer, C., Palmer, P.I., Geron, C., 2006. Estimates of global terrestrial isoprene emissions using MEGAN (model of emissions of gases and aerosols from nature). Atmos. Chem. Phys. 6 (11), 3181–3210. http://dx.doi.org/10.5194/acp-6-3181-2006.

Hersbach, H., Bell, B., Berrisford, P., Biavati, G., Horányi, A., Muñoz Sabater, J., Nicolas, J., Peubey, C., Radu, R., Rozum, I., Schepers, D., Simmons, A., Soci, C., Dee, D., Thépaut, J.-N., 2023. ERA5 hourly data on pressure levels from 1940 to present. Climate change service (C3S) climate data store (CDS). http://dx.doi.org/10.24381/cds.bd0915c6. (Accessed 1 September 2023).

Heus, T., van Heerwaarden, C.C., Jonker, H.J., Pier Siebesma, A., Axelsen, S., Van Den Dries, K., Geoffroy, O., Moene, A., Pino, D., De Roode, S., et al., 2010. Formulation of the dutch atmospheric large-eddy simulation (DALES) and overview of its applications. Geosci. Model Dev. 3 (2), 415–444. http://dx.doi.org/10.5194/gmd-3-415-2010.

Heusinkveld, V.W., van Hooft, J.A., Schilperoort, B., Baas, P., van de Wiel, B.J., et al., 2020. Towards a physics-based understanding of fruit frost protection using wind machines. Agricult. Forest. Meterol. 282, 107868. http://dx.doi.org/10.1016/j.agrformet.2019.107868.

Katul, G.G., Mahrt, L., Poggi, D., Sanz, C., 2004. One-and two-equation models for canopy turbulence. Bound.-Layer Meteorol. 113, 81–109. http://dx.doi.org/10.1023/B:BOUN.0000037333.48760.e5.

Kimura, K., Yasutake, D., Nakazono, K., Kitano, M., 2017. Dynamic distribution of thermal effects of an oscillating frost protective fan in a tea field. Biosyst. Eng. 164, 98–109. http://dx.doi.org/10.1016/j.biosystemseng.2017.09.010.

Klemp, J., Lilly, D., 1978. Numerical simulation of hydrostatic mountain waves. J. Atmos. Sci. 35 (1), 78–107. http://dx.doi.org/10.1175/1520-0469(1978)035<0078:NSOHMW>2.0.CO;2.

Lamichhane, J.R., 2021. Rising risks of late-spring frosts in a changing climate. Nature Clim. Change 11 (7), 554–555. http://dx.doi.org/10.1038/s41558-021-01090-x.

Lee, X., Barr, A.G., 1998. Climatology of gravity waves in a forest. Q. J. R. Meteorol. Soc. 124 (549), 1403–1419. http://dx.doi.org/10.1002/qj.49712454904.

Martinez, L., Leonardi, S., Churchfield, M., Moriarty, P., 2012. A comparison of actuator disk and actuator line wind turbine models and best practices for their use. In: 50th AIAA Aerospace Sciences Meeting Including the New Horizons Forum and Aerospace Exposition. p. 900. http://dx.doi.org/10.2514/6.2012-900.

Munters, W., Meneveau, C., Meyers, J., 2016. Turbulent inflow precursor method with time-varying direction for large-eddy simulations and applications to wind farms. Bound.-Layer Meteorol. 159, 305–328. http://dx.doi.org/10.1007/s10546-016-0127-z.

Patton, E., Finnigan, J., 2013. Canopy turbulence, Chap. 24. In: Handbook of Environmental Fluid Dynamics, Volume One. CRC Press, pp. 329–346.

Patton, E.G., Sullivan, P.P., Shaw, R.H., Finnigan, J.J., Weil, J.C., 2016. Atmospheric stability influences on coupled boundary layer and canopy turbulence. J. Atmos. Sci. 73 (4), 1621–1647. http://dx.doi.org/10.1175/JAS-D-15-0068.1.

Raupach, M., Coppin, P., Legg, B., 1986. Experiments on scalar dispersion within a model plant canopy part I: The turbulence structure. Bound.-Layer Meteorol. 35 (1), 21–52.

Ribeiro, A.C., De Melo-Abreu, J.P., Snyder, R.L., 2006. Apple orchard frost protection with wind machine operation. Agricult. Forest. Meterol. 141 (2–4), 71–81. http://dx.doi.org/10.1016/j.agrformet.2006.08.019.

Schuepp, P., 1993. Tansley review No. 59. Leaf boundary layers. New Phytol. 477–507. http://dx.doi.org/10.1111/j.1469-8137.1993.tb03898.x.

Shaw, R., Den Hartog, G., Neumann, H., 1988. Influence of foliar density and thermal stability on profiles of Reynolds stress and turbulence intensity in a deciduous forest. Bound.-Layer Meteorol. 45, 391–409. http://dx.doi.org/10.1007/BF00124010.

Torkelson, G., Price, T.A., Stoll, R., 2022. Momentum and turbulent transport in sparse, organized vegetative canopies. Bound.-Layer Meteorol. 184 (1), 1–24. http://dx.doi.org/10.1007/s10546-022-00698-6.

Troldborg, N., Sørensen, J.N., Mikkelsen, R., 2007. Actuator line simulation of wake of wind turbine operating in turbulent inflow. J. Phys. Conf. Ser. 75 (1), 012063. http://dx.doi.org/10.1088/1742-6596/75/1/012063.

van der Linden, S.J., Kruis, M.T., Hartogensis, O.K., Moene, A.F., Bosveld, F.C., van de Wiel, B.J., 2022. Heat transfer through grass: a diffusive approach. Bound.-Layer Meteorol. 184 (2), 251–276. http://dx.doi.org/10.1007/s10546-022-00708-7.

van Hooft, J.A., Baas, P., van Tiggelen, M., Ansorge, C., van de Wiel, B.J.H., 2019. An idealized description for the diurnal cycle of the dry atmospheric boundary layer. J. Atmos. Sci. 76 (12), 3717–3736. http://dx.doi.org/10.1175/JAS-D-19-0023.1.

Van Hooft, J.A., Popinet, S., Van Heerwaarden, C.C., Van der Linden, S.J., De Roode, S.R., Van de Wiel, B.J., 2018. Towards adaptive grids for atmospheric boundary-layer simulations. Bound.-Layer Meteorol. 167, 421–443. http://dx.doi.org/10.1007/s10546-018-0335-9.

van Ramshorst, J.G.V., Coenders-Gerrits, M., Schilperoort, B., van de Wiel, B.J.H., Izett, J.G., Selker, J.S., Higgins, C.W., Savenije, H.H.G., van de Giesen, N.C., 2020. Revisiting wind speed measurements using actively heated fiber optics: a wind tunnel study. Atmos. Meas. Tech. 13 (10), 5423–5439. http://dx.doi.org/10.5194/amt-13-5423-2020.

Van de Wiel, B., Moene, A., Hartogensis, O., De Bruin, H., Holtslag, A., 2003. Intermittent turbulence in the stable boundary layer over land. Part III: A classification for observations during CASES-99. J. Atmos. Sci. 60 (20), 2509–2522. http://dx.doi.org/10.1175/1520-0469(2003)060<2509:ITITSB>2.0.CO;2.

Van de Wiel, B.J., Vignon, E., Baas, P., Van Hooijdonk, I.G., Van der Linden, S.J., Van Hooft, J.A., Bosveld, F.C., de Roode, S.R., Moene, A.F., Genthon, C., 2017. Regime transitions in near-surface temperature inversions: a conceptual model. J. Atmos. Sci. 74 (4), 1057–1073. http://dx.doi.org/10.1175/JAS-D-16-0180.1.